Terrestrial structure-from-motion: spatial error analysis of roughness and morphology

Arved C. Schwendel[a*], David J. Milan[b]

[a]*School of Humanities, Religion & Philosophy, York St John University, Lord Mayor's Walk, York, YO31 7EX, UK*

**corresponding author: a.schwendel@yorksj.ac.uk*

[b]*Geography, Geology and Environment, University of Hull, Cottingham Road, Hull, HU6 7RX, UK*

d.milan@hull.ac.uk

Abstract

Structure-from-Motion (SfM) photogrammetry is rapidly becoming a key tool for morphological characterisation and change detection of the earth surface. This paper demonstrates the use of Terrestrial Structure-from-Motion (TSfM) photogrammetry to acquire morphology and roughness data at the reach-scale in an upland gravel-bed river. We quantify 1) spatially-distributed error in TSfM derived Digital Elevation Models (DEMs) and 2) identify differences in roughness populations acquired from TSfM photogrammetry versus TLS. We identify an association between local topographic variation and error in the TSfM DEM. On flatter surfaces (e.g. bar and terrace surfaces), the difference between the TSfM and TLS DEMs are generally less than ±0.1 m. However, in areas of high topographic variability (>0.4 m) such as berm or terrace edges, differences between the TSfM and TLS DEMs can be up to ±1 m. Our results suggest that grain roughness estimates from the TSfM point cloud generate values twice those derived from the TLS point cloud on coarse berm areas, and up to four-fold those derived from the TLS point cloud over finer gravel bar surfaces. This finding has implications when using SfM data to derive roughness metrics for hydrodynamic modelling. Despite the use of standard filtering procedures, noise pertains in the SfM DEM and the time required for its reduction might partially outweigh the survey efficiency using SfM. Therefore, caution is needed when SfM surveys are employed for the assessment of surface roughness at a reach-scale.

Keywords: Digital Elevation Model (DEM), error, roughness, SfM photogrammetry, Terrestrial Laser Scanning (TLS)

1. Introduction

The last ten years have seen a step-change in our ability to capture data remotely for geomorphological and hydrological applications (Entwistle et al., 2018). In fluvial geomorphology, Terrestrial Laser Scanning (TLS) has established itself as a key tool in the retrieval of data that allows detection of morphological change at high resolution at the reach-scale (Milan et al., 2007, Heritage and Milan, 2012; Wheaton et al., 2013), and in the characterisation of grain-scale topographic and roughness data over dry (Heritage and Milan, 2009; Hodge et al., 2009; Huang and Wang, 2012), and submerged (Smith et al., 2012; Miura and Asano, 2015) gravel surfaces capturing complex spatial patterns and changes after floods (Milan et al., 2009).

More recently, however, Structure-from-Motion (SfM) photogrammetry has emerged as a more cost-effective alternative to TLS with the ability to retrieve high density point cloud data for a range of geomorphological applications (Westoby et al., 2012; Fonstad et al., 2013; Smith et al., 2015; Dietrich, 2016; Carrvick and Smith, 2019), with most studies employing the technique from an unmanned drone (e.g. Marteau et al., 2017; Carbonneau and Dietrich, 2017; Entwistle and Heritage, 2017). Photogrammetry is well established in geomorphology (Lane et al., 1993; Barker, et al., 1997; Butler et al., 1998; Heritage et al., 1998; Chandler, 1999; Westaway et al., 2001), as a rapid survey technique that can be used to generate highly accurate grain-scale DEMs (Wang et al., 2015). SfM photogrammetry utilises mathematical models derived from early photogrammetry studies, including coplanarity and collinearity, and self-calibrating bundle adjustment (Kenefick et al., 1972; Faig, 1975; Ullman, 1979). The emergence of SfM photogrammetry has also been accompanied with the development of software (Snavely et al., 2006; Lague et al., 2013) capable of merging large digital image datasets, and the development of algorithms capable of producing dense point clouds from the imagery (Buscombe, 2016). SfM photogrammetry has been shown to produce reliable data for DEM production when survey design such as photo overlap, camera angle, distribution of ground control points, and environmental conditions is appropriate (see James and Robson, 2012 and James et al., 2017a for details) or corrections are applied during processing (James and Robson, 2014). Additional corrections such as for refraction at the water surface even allows construction of high quality DEMs from submerged areas of the bed (e.g. Woodget et al., 2015; Entwistle and Heritage, 2017; Dietrich, 2017). Retrieval of grain size and roughness data using SfM photogrammetry is a recent further development (Langhammer et al., 2017; Woodget and Austrums, 2017; Pearson et al., 2017; Woodget et al., 2018). The ability to retrieve morphology data from dry and submerged parts of the bed, and grain roughness information, allows for seamless surveys of the aquatic environment that may not be achieved using red-wavelength LiDAR systems, thus providing new opportunities for assessing spatial patterns in sediment budgets at the reach-scale, and improved hydrodynamic modelling within river systems.

Despite the increasing number of studies deploying SfM photogrammetry from unmanned drones, the challenges that exist when using this platform have received only limited attention. A number of potential issues exist (e.g. Duffy et al. 2017) as follows. 1) Access to a drone and a trained operator requires considerable initial cost and reliance on the availability of the drone operator. 2) The trained drone operator may not always be familiar with geomorphological or hydrological processes, and may therefore not capture the required information to the satisfaction of the geomorphologist. 3) Time needs to be taken for pre-flight planning of the site (Duffy et al., 2017). 4) Flights need to comply with local legislation, and permissions may not always be granted to fly at certain sites, and may take considerable time before being secured. It may therefore not be possible to retrieve data at short notice, as is often required in fluvial and hydrological projects (e.g. during or immediately after a flood event). Furthermore, drone flights are not possible at all in no-fly zones. 5) Weather conditions may not be suitable for drone flights. For example, it may not possible to deploy a drone during high wind speeds, yet still possible to take photographs form a terrestrial platform. 6) Shadow and sun angle effects caused by vegetation or coarse sediment can be problematic. 7) Drone battery life may limit photograph data retrieval, particularly when working in remote areas, where it may be difficult to recharge batteries. As a consequence, deployment of SfM photogrammetry from a terrestrial platform (TSfM) could offer a more reliable and cost-effective alternative in some instances. Indeed, some sites with steep slopes and near-vertical surfaces, such as river banks and landslides, might be more suitable for ground-based approaches (Westoby et al., 2012).

Although SfM has made it easier for non-specialists to use photogrammetry for landform measurement and change detection, this simplification has resulted in the introduction of new types of measurement errors, previously precluded by the strict application of camera calibration techniques and other controls in classical photogrammetry. Studies quantifying SfM photogrammetric errors, particularly at the reach-scale are lacking, largely due to the difficulties in acquiring suitable control datasets. Assessing the accuracy of SfM-derived point clouds and DEMs and appropriate error analyses are fundamental to the success of the approach in geomorphological change detection studies (e.g. Hugenholtz et al., 2013; Javernick et al., 2014; Entwistle and Heritage, 2017; James et al., 2017a; Cook, 2017), and grain size assessment (Westoby et al., 2015). Although SfM photogrammetry can have geometric distortion issues (e.g. James et al., 2017a), occlusion is less of an issue due to the multi-view geometry achieved thanks to the high number of photograph loci. In contrast, TLS does not suffer from systematic warping, although can suffer from occlusion issues, particularly when insufficient scans are taken with adequate overlap. In this paper we use a TLS-derived DEM as ground-truth data to assess the spatial distribution of SfM photogrammetric error. This paper aims to 1) interrogate spatial error in both morphology and grain roughness data, and 2) critically evaluate the ability of SfM photogrammetry with a terrestrial platform (TSfM) to capture morphology and roughness data.

2. Study site

This investigation focused on a 500 m reach of the Thinhope Burn, a small tributary catchment to the River South Tyne situated in the north Pennines in Cumbria, UK (OS National grid reference NY680550, latitude 54º 52’ 48.31” N, longitude 2º 31’ 09.57” W, 180-595 m Above Ordnance Datum, catchment area 12 km^2; Fig. 1). The river here is a sinuous single thread channel, displaying pool-riffle and rapid morphology, with a mean bed slope of 0.031 m m^{-1}. The role of high flow events is significant in this catchment, with coarse berm deposits with a typical D_{50} of 200 mm mobilised by infrequent catastrophic events (Macklin et al., 1992; Milan, 2012), and finer more mobile deposits (~D_{50} 30 mm) in the annually inundated areas of the channel making up the bed and point bars that are typically reworked by winter high flow events. The channel at this location has a Strahler (1952) stream order of 3, and drains a catchment underlain by Carboniferous sandstones, limestones, and shales, overlain by glacial diamicton. In the headwaters of the catchment, peat overlays the diamicton with depths of up to 2 m. The variety of grain sizes and morphological units in the reach provided an excellent opportunity to test the utility of TSfM photogrammetry to detect fluvial form and roughness.

The morphological development of Thinhope Burn over the Holocene and the more recent flood history has been reconstructed by Macklin et al. (1992), where three phases of incision were identified over the late Holocene, resulting in the formation of a series of terraces. Superimposed on these terraces were a series of boulder berm deposits, which Macklin et al. (1992) linked to 21 different large flood events occurring post 1766. In 2007, a large flood event caused significant mobilisation to the valley floor, fully reworking many of the old berms reported in Macklin et al. (1992), however depositing new berms and reconfiguring channel morphology (Milan, 2012; Milan and Schwendel 2019).

3. Methods

3.1. Field based approach

Smith (2015) reviewed TLS error sources, highlighting random and systematic instrument errors, error relating to the imaging geometry, the nature of the reflecting surface (e.g. shiny versus dull objects), environmental errors (e.g. atmospheric conditions), and methodological error (including registration and georeferencing errors) as possible sources. Despite this, TLS is still considered to currently be the best method available for producing accurate point clouds and DEMs, and has been shown to produce DEMs with millimetric accuracy which have been used for morphological and boundary roughness characterisation and change detection in a range of fluvial studies (e.g. Milan et al., 2007; Hodge et al., 2009; Williams et al., 2014). TLS has also been used to produce 'control' DEMs whereby the spatial error found in other survey techniques can be quantified (e.g. Heritage et al., 2009; Nadal-Romero et al., 2015). A GLS 2000 red-pulse TLS (Topcon Corporation, Tokyo, Japan) was used to gather sub-aerial data for the control DEM in this study. Eight overlapping scans were taken of the 500 m reach of Thinhope Burn from the valley sides and high terraces, where clear unobstructed views to the reach were available (Fig. 2). A series of overlapping tiepoints were surveyed, allowing the scans to be merged using Scanmaster software (Topcon Corporation, Tokyo, Japan). Topcon (2019) report a 'single point accuracy of 3.5 mm surveyed between 1 and 150 m (1σ) away from the scanner (as in this study), with a spot size of 4 mm at 20 m.

In union with the TLS survey, a total of 365 overlapping photographs were taken from 55 vantage points overlooking the channel (Fig. 2), using a Lumix TZ30 camera (Panasonic Corporation, Osaka, Japan). Thirty-six Ground Control Points (GCPs), scattered throughout the study site (Fig. 2), were used to help merge the photographs and produce a point cloud using Agisoft Photoscan software (Agisoft LLC, St. Petersburg, Russian Federation). Overlap between individual adjacent images was >70%, with all parts of the valley floor covered from at least nine camera stations. The average distance between the camera stations and the study area was 72.5 m with a total area of 0.036 km^2 covered. Both the tiepoints for the TLS survey and the GCPs were surveyed using a Leica dGPS 1200 (Leica Geosystems, Heerbrugg, Switzerland), allowing both point clouds to be georeferenced into the same coordinate system. The reported static accuracy of post-processed dGPS data is 5 mm + 0.5 ppm for horizontal, and is 10 mm + 0.5 ppm for vertical (Leica, 2008). Whilst the photogrammetric survey was carried out over a little more than one hour, the scanning required a full day.

3.2. Data analysis and processing

The images taken were aligned and underwent the Scale-Invariant-Feature-Transform (SIFT) algorithm using high accuracy setting in Photoscan. The sparse SFM point cloud (1777170 points) was subject to removal of points that did not suffice certain criteria (e.g. reprojection error) which reduced the sparse cloud by 7.5%. This resulted in an *RMSE* value of all tie points on all images of 1.76 pixels with an effective ground resolution of 8.93 mm per pixel, and ensured every point was projected based on the overlap of more than nine images. After application of the Multi-View Stereo (MVS) algorithm to the sparse SFM cloud, both, the dense TSFM and the TLS point cloud, underwent manual and automated low pass filtering (search radius 1 m, maximal variation in elevation 2 m and angle of <30° between a ground class point and a preliminary ground surface consisting of the lowest point in each search) in order to remove outlying points below and above the actual ground surface. The TSfM-derived point cloud was additionally classified by pixel colour in order to identify vegetation and points scattered below the coherent layer of ground surface points (i.e. the latter as identified by their grey gravel colour). This resulted in a point density of 1237 m^{-2} and 7322 m^{-2} for the TLS and TSfM clouds respectively. These clouds were subsequently reduced to the valley floor and the channel area. DEMs were produced in Surfer (Golden Software, Golden, USA) using triangulation with linear interpolation as the interpolation algorithm (Schwendel et al., 2012), with a grid spacing of 0.1 m for the entire reach and 0.05 m for separately investigated patches within the reach.

It is arguable whether remote sensing approaches actually measure grain size (e.g. Woodget and Austrums, 2017; Pearson et al., 2017; Woodget et al., 2018), as grains on a natural river bed are imbricated, partially buried and the particle edges partially obscured by neighbouring clasts. However, remote sensing approaches can measure roughness height of clasts, reflecting the degree of protrusion into the flow. Heritage and Milan (2009) demonstrated a linear relationship between twice the standard deviation of local elevation ($2\sigma_z$) and ground-truth measurements of clast c-axes, reflecting flow orientation of the primary axis in the streamwise direction exposing the shortest axis to the flow. We adopt this approach as a roughness measure in this study.

Grain roughness grids were produced through interrogating the point cloud by measuring the standard deviation of elevations in a moving window equivalent to the largest clast in the area of interest (Heritage and Milan, 2009). Within the entire reach the search radius was 0.8 m, while for the two selected coarser grained patches (S5 and S6) the search radius was 0.6 m, and for two finer-grained patches (S7 and S8) the search radius was 0.15 m. The standard deviation statistic is a measure of spread within the sample population, and is unaffected by sample size, thus allowing this statistic to be used on point clouds with different densities, and in situations where there are spatial differences in point density. However, standard deviation values become more stable with increasing sample size, and as such we deployed a minimum sample size of 30 points within the moving window. Populations of grain roughness values for these patches were produced through both survey methods, and the grain roughness populations were compared to identify differences.

3.3. Spatial error analysis

Spatial variation in difference (error) between the TSfM and TLS datasets were assessed by subtracting the latter from the former with the TLS surface regarded as reference (Heritage et al., 2009; Nadal-Romero et al., 2015). This permitted a visual assessment of the spatial patterns and magnitude of the differences throughout the reach (Fig. 3a). Cross-sections from the DEM of difference were also taken from a sub-reach containing several morphological features including bars, berms, terraces and banks, to further visualize the spatial differences in 2D.

The error inherent in DEMs for river survey datasets is known to be spatially variable, and linked to local topographic variation; with greater errors found at breaks of slope such as bank edges, as opposed to flatter bar surfaces (Heritage and Milan, 2009; Milan et al., 2011). We adopted the Milan et al. (2011) approach to characterize this effect through interrogating the relationship between local surface topographic variation and the local elevation difference between the two DEM surfaces. Local surface topographic (morphological) variability is defined by taking the local elevation standard deviation in a 0.8-m radius moving window over the point cloud, to produce a standard deviation of elevations grid (Fig. 4a). Elevation errors for each coordinate are established from the difference between TLS and TSFM elevations (Fig. 3a) and are used to create a spatially variable Level of Detection (LoD).

Greater topographic roughness values are generally found at breaks of slope in both clouds, however roughness is generally below 0.6 m with the TLS product having lower values (Fig. 4). Within the channel TLS derived roughness is generally less than 0.2 m, and elevated values are restricted to mid-channel bars throughout the reach and coarse flood-berms, particularly in the lower part of the reach. The TSfM product shows roughness of up to 0.5 m with high values in the central part and at a riffle in the lower part of the reach. Otherwise roughness of up to 0.2 m is found in similar locations than in the TLS cloud but spatially more extensive.

The plot of elevation error against local surface variation (Fig. 5a), established from digitising 2000 randomly distributed points from the TSfM-TLS difference grid, shows that on flatter surfaces (e.g. bar and terrace surfaces) with a local surface elevation variation of <±0.05 m, the difference between the TSfM and TLS DEMs is generally less than ±0.3 m. The variability around the mean error clearly increases within increasing topographic variability. In areas of high topographic variability (>0.4 m) such as berm or terrace edges, differences between the TSfM and TLS DEMs (error) can be up to ±3 m. Using the data in Fig. 5a, the standard deviation of elevation error was established for different classes of local surface variation. The relationship between standard deviation of elevation error and local surface variation classes is shown in Fig. 5b. The standard deviation of elevation error shows a strong power law relationship with local surface elevation variability (Fig. 5b). This relationship may be used to filter spatial error after two further steps (*sensu* Milan et al., 2011) are taken: 1) the regression equation (Fig. 5b) is applied to the grid of local topographic variability, produced here through taking the standard deviation of elevations in a 0.8-m moving window over the point cloud, to generate a spatial error grid, and 2) a spatially distributed root mean square error grid is produce through the application of

$$U_{crit} = t\sqrt{(\sigma_e)^2}$$

to the spatial error grid, where U_{crit} is the LoD; and σ_e is the standard deviation of elevation error, and *t* is the critical *t*-value at the chosen confidence level here set at a value of 1.96 (2σ), in which case the confidence limit is equal to 95%.

4. Results

4.1. Digital Elevation Models

The surface of difference between the DEMs based on TSfM data and TLS data (Fig. 3) shows the highest deviation near the lateral edges of the valley floor and the channel as well as on the inside of some bends. Field observations and photographs identify these areas as locations where the channel actively erodes valley slopes and terraces, and sudden breaks in slope such as channel banks and terraces edges. Actively eroding slopes and terraces (marked A in Fig. 3a) are underestimated in the TSfM DEM, in particular the grassy surface of slumped blocks. Similarly, actively eroding banks (marked B in Fig. 3a) tend to be lower and therefore appear more retreated in the TSfM dataset. Some former cut-banks, now protected by bars or berm deposits (marked C in Fig. 3a), also show this pattern. In contrast, banks dominated by coarse, bulldozed cobbles and boulders (marked D in

Fig. 3a) appear to be overestimated in elevation and less retreated in the TSfM DEM. This also applies to currently inactive coarse bar deposits such as the berms marked E in Fig. 3a. The maximum vertical deviation between the DEMs is up to 4 m. Fig. 3b demonstrates how the majority of error has been removed following the filtering procedure; based upon the relationship between elevation error (difference between TSfM and TLS DEMs) and topographic variability (local morphological roughness). Most of the differences evaluated here are within the topography-dependant LoD and that genuine differences between the two DEMs are within ±1 m. Within the channel the deviations are variable, usually within a range of 0.1 m around 0, except for a coarse substrate area showing substantial underestimation of the TSfM DEM in the centre of the reach (marked F in Fig. 3a). Open water surfaces are represented generally lower in the TSfM DEM. Homogeneous gravel bars (marked G in Fig. 3a) appear to show the least deviation between the two DEMs.

The long-profile for the lower part of the study reach (Fig. 6) shows a more 'noisy' profile for the TSfM data compared with the TLS DEM, particularly at riffles. Cross-section A–A' traverses a series of flood berms and a point bar and ends at a slumping hillslope. The strongest deviations between the two DEMs occur in the North on vegetated berms but there appears to also be a systematic shift to the South West of the TSfM DEM which is also apparent in Section C–C' (Fig. 6). Section B–B' is located between two terraces and shows the highest deviation at the terrace edges and in an area with coarse flood deposits to the East of the current channel. Section C–C' shows considerable underestimation of the surface elevation by the TSfM DEM in an area dominated by a riffle. In addition, the partially vegetated surface of a terrace in the SW and a boulder berm show much higher variability for this DEM. Section D–D’ traverses the channel from the slumping valley side, over a relatively smooth point-bar onto a terrace. Despite the vegetation on the latter, here both DEMs are largely in good agreement. However, in this section and others, the angle of nearly vertical slopes subject to erosion appears to be greater in the TLS DEM compared to the TSfM product. Slopes extracted from the TSfM product appear to be more retreated and have less steep slopes at A’, B’ and D while the opposite, more stable, side may show a steeper slope (e.g. at B).

4.2. Roughness comparison

Accurate measurement of boundary roughness is needed as input to hydrodynamic modelling, and techniques such as TLS and TSfM now allow fully spatially distributed roughness information to be included in flow simulations. Here we explore the difference in roughness characterisation using the two techniques. Grain roughness populations were investigated at four patches representative of different morphological units. Patch S5 (Fig. 7), a boulder berm, shows similar spatial distribution of roughness in the southern half between both DEMs, while in the northern part there are three distinct zones with elevated roughness in the TSfM DEM. Patch S6 covers a boulder berm deposited in 2007 (Fig. 8). The measured roughness is of similar magnitude in both DEMs (Table 1) with two zones of elevated roughness present in the TSfM DEM (a North-East edge and a North–South aligned ridge) that are not shown in the TLS product. The differences between the two DEMs are shown as a shift of the maximum frequency to higher roughness and a bimodal distribution for the SFM product which account for these zones (Fig. 9, Table 1).

The two fine-grained patches S7 and S8 differ in their roughness measurement between the two approaches (Figs. 10 and 11). The TLS DEM is much smoother than the TSfM DEM and the spatial distribution of roughness does not match. The TSfM DEMs show more variability in roughness which is reflected in their relatively wide frequency distribution (Fig. 9). In contrast, the roughness range of the TLS DEMs is rather narrow and centred at considerably lower roughness compared to the TSfM DEM (Table 1).

5. Discussion

The differences between DEMs generated from TSfM photogrammetry and TLS are spatially variable and showed an association with local topographic variability. Substantial DEM differences were restricted to small areas following error filtering. While the degree of vegetation appears to be important, a clear attribution of these differences to specific morphological units was not evident. The channel and most bars show little detectable difference which reflects the quality of the DEMs in areas of little topographic variability. Even in the wet channel, differences of more than a few centimetres were only detected in areas where their magnitude and their incongruence with geomorphological units (riffle) suggest outlying points that escaped the filtering process of the TSfM point cloud (F in Fig. 3a). The level of detection in the channel was rather low due to it being derived from a comparison with the TLS dataset which shows very little topographic variation within the channel (Fig. 4) and contains patches of water, detected as very smooth surfaces (Fig. 6). Therefore, the general minor differences between the two DEMs are remarkable given the difficulties introduced by the differential penetration of water surfaces, reflection and refraction (Woodget et al., 2015). The different representation of water surfaces, also evident in some parts of the long-profile (Fig. 6), can be attributed to the reconstruction of some sub-aqueous surfaces with the TSfM approach while red laser wavelengths are absorbed in water (Cook, 2017). A detailed assessment of the suitability of the two techniques for measurement of topography and roughness in sub-merged areas is beyond the scope of this paper, and ideally these would have been excluded from the analysis. While manually blanking patches of water surface in the DEMs could address this issue, in shallow gravel-bed reaches of this size this is very time consuming and can be impractical. Because the true-colour TSfM pixel might not allow distinction between shallow submerged channel and dry channel, the use of the intensity of laser signal returns to detect the water edge might be preferable (Flener et al., 2013). However, in this instance differences between the DEMs at patches of water were of small magnitude not exceeding the level of detection, hence light penetration issues in the submerged areas appear to have not significantly reduced DEM accuracy.

In contrast to the channel, more elevated bars and berms, terraces and actively eroding slopes coupled to the channel showed in places substantial differences of up to 1 m between the two DEMs (Fig. 3). Locations affected can be separated in two categories: areas affected by vegetation and breaks in slopes. Foliage of vegetation can lead to differential penetration of light and therefore will affect surveys utilising light waves (Heritage and Hetherington, 2007; Cook, 2017). This study suggests that vegetation was a cause of difference between the datasets as well as topographic variability, however we are unable to quantify this in the present investigation. Although the area of interest of this study largely consists of unvegetated river channel, bars and banks, some of the stable floodplain and terraces were covered in short herbaceous vegetation. The filters applied to the point clouds eliminated high points but were unable to exclude gradual transition from a bare surface to low vegetation (Cook, 2017; James et al., 2017a). Although vegetated surfaces will always be problematic for TSfM and TLS surveys (Lane, 2000; Castillo et al., 2012; Tonkin et al., 2014; Cook, 2017), fresh deposition of sediment between vegetation or the gradual encroachment of plants on bars mean that the presence of vegetation in peripheral areas cannot always be excluded in geomorphological studies.

The greatest elevation differences between the two DEMs are located at breaks in slope such as eroding terrace edges, valley slopes and banks but they exceed the spatially variable level of genuine detection based on the local topographic variation only in a small number of places (Fig 3). The reason for significant elevation differences can be found in different representation of slope angles: actively eroding slopes appear steeper in the TLS DEM, while stable breaks in slope are often shown as steeper in the TSfM DEM (Fig. 3). Deviations at steep slopes and near vertical surfaces are a common problem, particularly in aerial photogrammetry (Lague et al., 2013; Carbonneau and Dietrich, 2017; Cook, 2017; Huang et al., 2017). Since the slopes in the two DEMs have common toe points, these deviations are not likely due to a uni-directional relative shift in DEM position, for example due to GCP precision, or tilt but rather a result of distortion during the SFM-multi-view stereo process (Fonstad et al., 2013; James et al., 2017a). Smoothing of breaks in slopes and misrepresentation of slope angles in SfM DEMs, e.g. as reported by Kolzenburg et al. (2016), can be attributed to filtering processes during image matching (James and Robson, 2017b). This study used a variety of camera positions and camera angles from the terrestrial vantage points to minimise this problem. The slopes with considerable differences are distributed throughout the DEM thus localised distortion or issues with individual images or GCPs can be excluded. Conversely, steep slopes facing up-valley or down-valley and thus captured from both valley sides are equally affected as slopes mostly captured only from one valley side. James et al. (2017b) found systematic differences between SfM and TLS DEMs along steep slopes which indicate horizontal error in the relative georeferencing of the DEMs, and indicate that cloud-to-cloud comparison in combination with photogrammetric precision estimates can to some extent account for this error. If image capture or processing issues can be ruled out, the different representation of slope shape could potentially also be related to characteristics of actively eroding slopes such as roughness and colour which may be relevant during the SFM image matching process.

As for the entire DEM, within the channel, the variation between the two DEMs appears to increase with topographic variation. Although DEM accuracy generally tends to show this tendency (e.g. Milan et al., 2011, Cook, 2017 but not Kolzenburg et al., 2016), the steepness of the regression line (Fig. 5b) suggests that the TSfM DEM differs not only at the discussed, significant breaks in slopes, but generally in areas with high topographic roughness.

By using twice the standard deviation of elevation values within a moving window equivalent to the largest clast, Heritage and Milan (2009) were able to show how dense point clouds may be used to provide bar-scale grain roughness information, and showed relationships between the roughness and grain size. Due to the purely comparative nature of this study, only one standard deviation is reported here. The measured roughness over the entire reach compounds types of roughness at a range of scales from skin (surface) roughness of large boulders, over grain roughness, to vegetation and bedform roughness. Gravel-cobble bar surfaces such as patches 7 and 8 (Figs. 10 and 11) provide the opportunity to compare the assessment of grain roughness based on the two datasets. The ratio of respective percentiles of roughness height is up to four with barely any similarity between the spatial distribution of roughness. Although both sets of frequency distributions (Fig. 9) retain their single-modal shape, there is a distinct shift in modal values and spread.

James and Robson (2017b) suggest that the representation of small roughness elements can be affected by filtering and smoothing processes during the image matching process (Hirschmuller, 2008). At the coarser patches S5 and S6 (Figs. 7 and 8), the difference between the roughness representation between the two DEMs is smaller, i.e., there is some agreement in spatial distribution of roughness elements. Both patches encompass boulder berms deposited in the 2007 flood (Milan, 2012). Patch S5 was deposited on the inside of a bend, and its roughness has been affected since then by gradual covering in finer sediment and partially stripping of the latter by smaller floods. Its mean roughness height derived from the TLS and TSfM datasets of respectively 228 mm and 452 mm substantially exceed the mean b-axis length of a visually very similar berm situated nearby that has been reworked in 2007 (130 mm, berm 2 in Milan, 2012). Given that roughness height is better correlated with the smaller c-axis length (Heritage and Milan, 2009) and standard deviation of elevation may be much lower than measured particle size (Brasington et al., 2012), this shows a considerable potential overestimation of measured roughness despite the fine sediment cover. Since 2007 patch S6 has been subject to in-channel reworking (Milan and Schwendel, 2019) of fines and thus has developed a bimodal grain size distribution which is shown by both survey methods (Fig. 9). For both coarse patches, the mean roughness height of the SFM dataset is approximately twice that of the TLS DEM with a remarkable consistency between percentiles (Table 1) and their frequency distributions are of similar character, e.g., are comparable after a simple exponential transformation. This shows that the representation of grain roughness scales with grain size, although it remains unclear to which extent the differences are due to systematic smoothing within the TSfM process or may be attributed to higher random noise in the TSfM point cloud (Cook, 2017) as evident in the roughness frequency distributions (Fig. 9).

Over the entire valley floor, both surveys agreed in identifying highest roughness at areas of vegetation, at breaks in slope and coarse boulder berms (Fig. 5). While in the first two locations, the values are an artefact of the interrogation method or due to differential penetration of the vegetation cover (Lane, 2000; Castillo et al., 2012; Tonkin et al., 2014), in the latter location they may represent actual grain roughness. The gradual nature of encroachment of vegetation onto bare surfaces as well as sediment deposited on top of vegetation provides difficulties for the exclusion of vegetation from the analysis. Investigation focussing on morphometric changes also cannot neglect these marginal sites.

6. Conclusions

The comparison channel DEMs derived from interpolated point clouds based on TSfM and TLS surveys showed that on smooth gravel bars and terrace surfaces, the vertical difference does not exceed 0.3 m which reduces to 0.1 m after a threshold of genuine change detection is applied. Here the surface roughness, assessed as the standard deviation of local elevation, is considerably higher in the TSfM DEM compared with the TLS DEM suggesting that removal of random noise by filtering remains a key issue in order to make full use of the survey efficiency of the technique. Caution should be exercised when using TSfM point clouds to provide roughness data for hydrodynamic modelling; perhaps through field calibration. In areas of higher relief such as breaks in slopes, roughness estimates vary most between the two approaches and differences between the DEMs can approach 1 m on terrace edges or slips on the valley sides. In these areas inaccuracies introduced by differential penetration of vegetation play a role as well, and might be of higher relative magnitude than noise. This is supported by the similarities in the roughness frequency distributions in coarse grained patches. The representation of near vertical surfaces varies between the two DEMs, in particular at the upper edge which could be improved by the use of direct comparison of point clouds. This research highlights that in fluvial landscapes, where spatial heterogeneity of relief, surface material and roughness is high, finding suitable filtering processes for point clouds is challenging. Despite using a range of point cloud filtering processes and high-quality settings in the analysis software, the TSfM dataset does not achieve comparable results to the TLS DEM in key areas of the reach. Thus, for the accurate assessment of surface roughness on a reach-scale the higher surveying time using the TLS technique might be in part offset by shorter data processing time.

References

Barker, R., Dixon, L. and Hooke, J., 1997. Use of terrestrial photogrammetry for monitoring and measuring bank erosion. Earth Surface Processes and Landforms, 22(13), 1217-1227.

Brasington, J., Vericat, D., Rychkov I., 2012. Modeling river bed morphology, roughness, and surface sedimentology using high resolution terrestrial laser scanning. Water Resources Research, 48, W11519. doi: doi:10.1029/2012WR012223

Buscombe, D., 2016. Spatially explicit spectral analysis of point clouds and geospatial data. Computers & Geosciences, 86, pp.92-108.

Butler, J.B., Lane, S.N. and Chandler, J.H., 1998. Assessment of DEM quality for characterizing surface roughness using close range digital photogrammetry. The Photogrammetric Record, *16*(92), pp.271-291.

Carbonneau, P.E. and Dietrich, J.T., 2017. Cost-effective non-metric photogrammetry from consumer-grade sUAS: implications for direct georeferencing of structure from motion photogrammetry. Earth Surface Processes and Landforms, 42(3), pp.473-486.

Carrivick, J.L. and Smith, M.W., 2019. Fluvial and aquatic applications of Structure from Motion photogrammetry and unmanned aerial vehicle/drone technology. Wiley Interdisciplinary Reviews: Water, 6(1), p.e1328.

Castillo, C., Pérez, R., James, M.R., Quinton, N.J., Taguas, E.V., Gómez, J.A., 2012. Comparing the accuracy of several field methods for measuring gully erosion. Soil Science Society of America Journal, 76. pp.1319–1332. DOI:10.2136/sssaj2011.0390.

Chandler, J., 1999. Effective application of automated digital photogrammetry for geomorphological research. Earth Surface Processes and Landforms, 24(1), pp.51-63.

Cook, K.L., 2017. An evaluation of the effectiveness of low-cost UAVs and structure from motion for geomorphic change detection. Geomorphology, *278*, pp.195-208.

Dietrich, J.T., 2016. Riverscape mapping with helicopter-based Structure-from-Motion photogrammetry. Geomorphology, 252, 144-157.

Dietrich, J.T., 2017. Bathymetric structure-from-motion: extracting shallow stream bathymetry from multi-view stereo photogrammetry. Earth Surface Processes and Landforms, 42(2), 355-364.

Duffy, J.P., Cunliffe, A.M., DeBell, L., Sandbrook, C., Wich, S.A., Shutler, J.D., Myers-Smith, I.H., Varela, M.R. and Anderson, K., 2018. Location, location, location: considerations when using lightweight drones in challenging environments. Remote Sensing in Ecology and Conservation, 4(1), pp.7-19.

Entwistle, N.S. and Heritage, G., 2017. An evaluation DEM accuracy acquired using a small unmanned aerial vehicle across a riverine environment. International Journal of New Technology and Research, 3(7), pp.43-48.

Entwistle, N., Heritage, G.L., Milan, D.J. 2018. Recent Remote Sensing Applications for Hydro and Morphodynamic Monitoring and Modelling. Earth Surface Processes and Landforms, 43, pp.2283-2291.

Faig, W., 1975. Calibration of close-range photogrammetric systems: Mathematical formulation. Photogrammetric engineering and remote sensing, 41(12), 1479-1486.

Fonstad, M.A., Dietrich, J.T., Courville, B.C., Jensen, J.L., Carbonneau, P.E., 2013. Topographic structure from motion: a new development in photogrammetric measurement. Earth Surface Processes and Landforms, 38(4), pp.421-430.

Flener, C., Vaaja, M., Jaakkola, A., Krooks, A., Kaartinen, H., Kukko, A., Kasvi, E., Hyyppä, H., Hyyppä, J., Alho, P., 2013. Seamless Mapping of River Channels at High Resolution Using Mobile LiDAR and UAV-Photography. Remote Sensing, 5(12), pp.6382-6407.

Heritage, G.L., Fuller, I.C., Charlton, M.E., Brewer, P.A. and Passmore, D.P., 1998. CDW photogrammetry of low relief fluvial features: accuracy and implications for reach-scale sediment budgeting. Earth Surface Processes and Landforms, 23(13), 1219-1233.

Heritage, G. and Hetherington D., 2007. Towards a protocol for laser scanning in fluvial geomorphology. Earth Surface Processes and Landforms 32(1), pp.66-74.Heritage, G.L. and Milan, D.J., 2009. Terrestrial laser scanning of grain roughness in a gravel-bed river. Geomorphology, 113(1), pp.4-11.

Heritage, G.L., Milan, D.J., Large, A.R., Fuller, I.C., 2009. Influence of survey strategy and interpolation model on DEM quality. Geomorphology, 112(3), pp.334-344.Hodge, R., Brasington, J., Richards, K., 2009. In situ characterization of grain-scale fluvial morphology using Terrestrial Laser Scanning. Earth Surface Processes and Landforms, 34(7), pp.954-968.

Hirschmuller, H., 2008. Stereo processing by semiglobal matching and mutual information. IEEE Transactions on Pattern Analysis and Machine Intelligence 30, 328–341. DOI:10.1109/Tpami.2007.1166.

Huang, G.H. and Wang, C.K., 2012. Multiscale geostatistical estimation of gravel-bed roughness from terrestrial and airborne laser scanning. IEEE Geoscience and Remote Sensing Letters, 9(6), 1084-1088.

Huang, H., Long, J., Lin, H., Zhang L., Yi, W., Lei, B., 2017. Unmanned aerial vehicle based remote sensing method for monitoring a steep mountainous slope in the Three Gorges Reservoir, China. Earth Science Informatics 10(3), pp.287-301.

Hugenholtz, C.H., Whitehead, K., Brown, O.W., Barchyn, T.E., Moorman, B.J., LeClair, A., Riddell, K., Hamilton, T., 2013. Geomorphological mapping with a small unmanned aircraft system (sUAS): Feature detection and accuracy assessment of a photogrammetrically-derived digital terrain model. Geomorphology, 194, pp.16-24.

James, M.R. and Robson S., 2012. Straightforward reconstruction of 3D surfaces and topography with a camera: Accuracy and geoscience application. Journal of Geophysical Research: Earth Surface 117: F03017. doi: 10.1029/2011JF002289

James, M.R. and Robson S., 2014. Mitigating systematic error in topographic models derived from UAV and ground-based image networks. Earth Surface Processes and Landforms 39(10): 1413-1420. DOI: 10.1002/esp.3609

James, M.R., Robson, S., d'Oleire-Oltmanns, S., Niethammer, U., 2017a. Optimising UAV topographic surveys processed with structure-from-motion: Ground control quality, quantity and bundle adjustment. Geomorphology, 280, pp.51-66.

James, M.R., Robson, S., Smith, M.W., 2017b. 3-D uncertainty-based topographic change detection with structure-from-motion photogrammetry: precision maps for ground control and directly georeferenced surveys. Earth Surface Processes and Landforms, 42, 1769-1788. doi: 10.1002/esp.4125

Javernick, L., Brasington, J. and Caruso, B., 2014. Modeling the topography of shallow braided rivers using Structure-from-Motion photogrammetry. Geomorphology, 213, pp.166-182.

Kenefick, J.F., Gyer, M.S. and Harp, B.F., 1972. Analytical self-calibration. Photogrammetric Engineering, 38(11), 1117-1126.

Kolzenburg, S., Favalli, M., Fornaciai, A., Isola, I., Harris, A.J.L., Nannipieri, L., Giordano, D., 2016. Rapid Updating and Improvement of Airborne LIDAR DEMs Through Ground-Based SfM 3-D Modeling of Volcanic Features. IEEE Transactions on Geoscience and Remote Sensing, 54(11). pp.6687-6699.

Lague, D., Brodu, N. and Leroux, J., 2013. Accurate 3D comparison of complex topography with terrestrial laser scanner: Application to the Rangitikei canyon (NZ). ISPRS journal of photogrammetry and remote sensing, 82, pp.10-26.

Lane, S.N., Richards, K.S. and Chandler, J.H., 1993. Developments in photogrammetry; the geomorphological potential. Progress in Physical Geography, 17(3), pp.306-328.

Lane, S.N., 2000. The measurement of river channel morphology using digital photogrammetry. The Photogrammetric Record, 16, pp.937–961.

Langhammer, J., Lendzioch, T., Miřijovský, J., Hartvich, F., 2017. UAV-Based Optical Granulometry as Tool for Detecting Changes in Structure of Flood Depositions. Remote Sensing, 9(3), p.240.

Leica Geosystems, A.G., 2008. Leica GPS1200 Series Technical Data.

Macklin, M.G., Rumsby, B.T., Heap, T., 1992. Flood alluviation and entrenchment: Holocene valley-floor development and transformation in the British uplands. Geological Society of America Bulletin, 104(6), pp.631-643.

Marteau, B., Vericat, D., Gibbins, C., Batalla, R.J., Green, D.R., 2017. Application of Structure-from-Motion photogrammetry to river restoration. Earth Surface Processes and Landforms, 42(3), pp.503-515.

Milan, D.J., 2009. Terrestrial laser scan-derived topographic and roughness data for hydraulic modelling of gravel-bed rivers (pp. 133-146). Wiley-Blackwell: Oxford, UK.

Milan, D.J., 2012. Geomorphic impact and system recovery following an extreme flood in an upland stream: Thinhope Burn, northern England, UK. Geomorphology, 138(1), pp.319-328.

Milan, D.J. and Heritage, G.L., 2012. LiDAR and ADCP use in gravel bed rivers: Advances since GBR6. In Church, M., Biron, P. and Roy, A. (eds) Gravel-bed rivers: Processes, Tools, Environments, John Wiley & Sons, Chichester, pp286-302.

Milan, D.J., Heritage, G.L., Entwistle, N., 2009. Detecting grain roughness change and sorting patterns in a gravel-bed river using terrestrial laser scanning. In Proceedings of the 33rd Congress of the International Association for Hydraulic Engineering and Research (IAHR), pp. 10-14.

Milan, D.J., Heritage, G.L., Hetherington, D., 2007. Application of a 3D laser scanner in the assessment of erosion and deposition volumes and channel change in a proglacial river. Earth Surface Processes and Landforms, 32(11), pp.1657-1674.

Milan, D.J., Heritage, G.L., Large, A.R., Fuller, I.C., 2011. Filtering spatial error from DEMs: Implications for morphological change estimation. Geomorphology, 125(1), pp.160-171.

Milan, D.J. and Schwendel, A.C. 2019. Long-term channel response to a major flood in an upland gravel-bed river. Proceedings of the 38th IAHR World Congress September 1-6, 2019, Panama City, Panama.

Miura, N. and Asano, Y., 2016. Effective acquisition protocol of terrestrial laser scanning for underwater topography in a steep mountain channel. River Research and Applications, 32(7), 1621-1631.

Nadal-Romero, E., Revuelto, J., Errea, P. and López-Moreno, J.I., 2015. The application of terrestrial laser scanner and SfM photogrammetry in measuring erosion and deposition processes in two opposite slopes in a humid badlands area (central Spanish Pyrenees). Soil, 1(2), 561.

Pearson, E., Smith, M., Klaar, M., Brown, L., 2017. Can high resolution topographic surveys provide reliable grain size estimates in gravel bed rivers?. Geomorphology, 293. pp.143-155

Snavely, N., Seitz, S.M., Szeliski R., 2006. Photo tourism: Exploring photo collections in 3D, ACM Transactions on Graphics, 25, pp.835–846. doi:10.1145/1141911.1141964.

Schwendel, A.C., Fuller, I.C. and Death, R.G. (2012). Assessing DEM interpolation methods for effective representation of upland stream morphology for rapid appraisal of bed stability. River Research and Applications, 28(5), pp.567-584. doi: 10.1002/rra.1475

Smith, M., Vericat, D., Gibbins, C., 2012. Through-water terrestrial laser scanning of gravel beds at the patch scale. Earth Surface Processes and Landforms, 37(4), pp.411-421.

Smith, M.W., 2015. Direct acquisition of elevation data: Terrestrial Laser Scanning. Geomorphological Techniques. British Society for Geomorphology.

Smith, M.W., Carrivick, J.L. and Quincey, D.J., 2016. Structure from motion photogrammetry in physical geography. Progress in Physical Geography, 40(2), pp.247-275.

Strahler, A.N., 1952. Hyposometric area–altitude. analysis of erosional topography. Geological Society of America Bulletin, 63, pp.1117-1142.

Tonkin, T.N., Midgley, N.G., Graham, D.J., Labadz,J.C., 2014. The potential of small unmanned aircraft systems and structure-from-motion for topographic surveys: A test of emerging integrated approaches at Cwm Idwal, North Wales. Geomorphology, 226, pp.35-43.

Topcon 2019. GLS-2000 Specifications. https://www.topconpositioning.com/mass-data-and-volume-collection/laser-scanners/gls-2000#panel-product-specifications (accessed 6th Jan 2019)

Ullman, S., 1979. The interpretation of structure from motion. Proc. Royal Society London, Ser. B, 203, pp. 405–426. doi:10.1098/rspb.1979.0006.

Wang, C.K., Chung, J.T. and Lin, Y.L., 2015. DEM Measurements of a gravel-bed surface using two scales of images. The Photogrammetric Record, 30(152), pp.387-401.

Westaway, R.M., Lane, S.N. and Hicks, D.M., 2001. Remote sensing of clear-water, shallow, gravel-bed rivers using digital photogrammetry. Photogrammetric Engineering and Remote Sensing, 67(11), pp.1271-1282.

Westoby, M.J., Brasington, J., Glasser, N.F., Hambrey, M.J., Reynolds, J.M., 2012. 'Structure-from-Motion' photogrammetry: A low-cost, effective tool for geoscience applications. Geomorphology, 179, pp.300-314.

Westoby, M.J., Dunning, S.A., Woodward, J., Hein, A.S., Marrero, S.M., Winter, K., Sugden, D.E., 2015. Sedimentological characterization of Antarctic moraines using UAVs and Structure-from-Motion photogrammetry. Journal of Glaciology, 61(230), pp.1088-1102.

Wheaton, J.M., Brasington, J., Darby, S.E., Kasprak, A., Sear, D., Vericat, D., 2013. Morphodynamic signatures of braiding mechanisms as expressed through change in sediment storage in a gravel-bed river. Journal of Geophysical Research: Earth Surface, 118(2), pp.759-779.

Williams, R.D., Brasington, J., Vericat, D., Hicks, D.M., 2014. Hyperscale terrain modelling of braided rivers: fusing mobile terrestrial laser scanning and optical bathymetric mapping. Earth Surface Processes and Landforms, 39(2), pp.167-183.

Woodget A.S. and Austrums R., 2017. Subaerial gravel size measurement using topographic data derived from a UAV-SfM approach. Earth

Surface Processes and Landforms, 42: pp.1434–1443. doi: 10.1002/esp.4139.

Woodget A.S., Carbonneau P.E., Visser F., Maddock I.P., 2015. Quantifying submerged fluvial topography using hyperspatial resolution UAS imagery and structure from motion photogrammetry. Earth Surface Processes and Landforms 40(1): pp.47-64.

Woodget A.S., Fyffe C., Carbonneau P.E., 2018. From manned to unmanned aircraft: Adapting airborne particle size mapping methodologies to the characteristics of sUAS and SfM. Earth Surface Processes and Landforms, 43, pp.857-870. doi: 10.1002/esp.4285.

Figure captions

Fig. 1. The South Tyne catchment (dashed line shows its devide) in the North Pennines with the River South Tyne and its major tributaries (thick line) and smaller tributaries (thin lines). The location of the study reach is shown by a point within the Thinhope Burn sub-catchment (shaded rectangle). The inset on the right indicates the location of the catchment within the boundaries of the UK.

Fig. 2. DEM of the studied reach with position of TLS stations (open circles), camera positions (filled circles), ground control points for TSfM (open squares) and the location of the patches P5 to P8. The full 500 m long study reach is highlighted by the boundary line.

Fig. 3. DEM of difference (SFM – TLS) of the study reach at Thinhope Burn. (a) For highlighting the raw differences without a Level of Detection (LoD) and (b) with a spatially variable LoD applied. Grey areas indicate no difference. The annotated letters are referred to in the text. Coordinates are given in British National Grid (units are metres).

Fig. 4. Surface topographic roughness height (in metres) derived from the a) TLS and b) SFM dense point clouds by assessing the standard deviation of local topographic elevation within a 0.8 m search radius. Coordinates are given in British National Grid (units are metres).

Fig. 5. Error assessment between the TLS and TSfM DEMs based on 2000 randomly selected points, (a) differences between the two DEMs versus local surface elevation within a 0.8 m radius, and (b) standard deviation of the difference between the DEMs plotted against local topographic variability.

Fig. 6. Transverse and longitudinal channel cross-sections of the TLS and TSfM DEMs.

Fig. 7. Surface roughness (in metres) of the TLS and TSfM DEMs as one standard deviation of local topographic variability using a search radius of 0.6 m at patch S5 (location within the study reach given in Fig. 2), a boulder berm deposited in 2007 as illustrated in the inset photograph. Coordinates are given in British National Grid (units are metres).

Fig. 8. Surface roughness (in metres) of the TLS and TSfM DEMs as one standard deviation of local topographic variability using a search radius of 0.6 m at patch S6 (location within the study reach given in Fig. 2), a boulder berm deposited in 2007 as illustrated in the inset photograph. Coordinates are given in British National Grid (units are metres).

Fig. 9. Frequency distributions of roughness height derived from the TLS and TSfM DEMs at the patches S5 to S8.

Fig. 10. Surface roughness (in metres) of the TLS and TSfM DEMs as one standard deviation of local topographic variability using a search radius of

0.15 m at patch S7 (location within the study reach given in Fig. 2), a lateral gravel bar as illustrated in the inset photograph. Coordinates are given in British National Grid (units are metres).

Fig. 11. Surface roughness (in metres) of the TLS and TSfM DEMs as one standard deviation of local topographic variability using a search radius of 0.15 m at patch S8 (location within the study reach given in Fig. 2), a gravel bar as illustrated in the inset photograph. Coordinates are given in British National Grid (units are metres).

Table 1. Percentiles of a grain roughness measure (in cm) derived from the standard deviation of elevation within two coarse-grained patches (S5 and S6) and two fine-grained patches (S7 and S8) at Thinhope Burn.

	Patch S5		**Patch S6**		**Patch S7**		**Patch S8**	
	TSfM	TLS	TSfM	TLS	TSfM	TLS	TSfM	TLS
25^{th} percentile	16.0	8.3	14.5	9.4	5.8	1.1	5.2	1.7
50^{th} percentile	22.6	11.4	22.7	11.7	7.4	1.6	6.5	2.0
75^{th} percentile	30.3	16.1	30.2	16.2	10.8	2.0	7.5	2.3
99^{th} percentile	57.4	29.8	52.5	34.0	22.8	4.2	10.7	3.8

Figure 1 (Colour)
Click here to download high resolution image

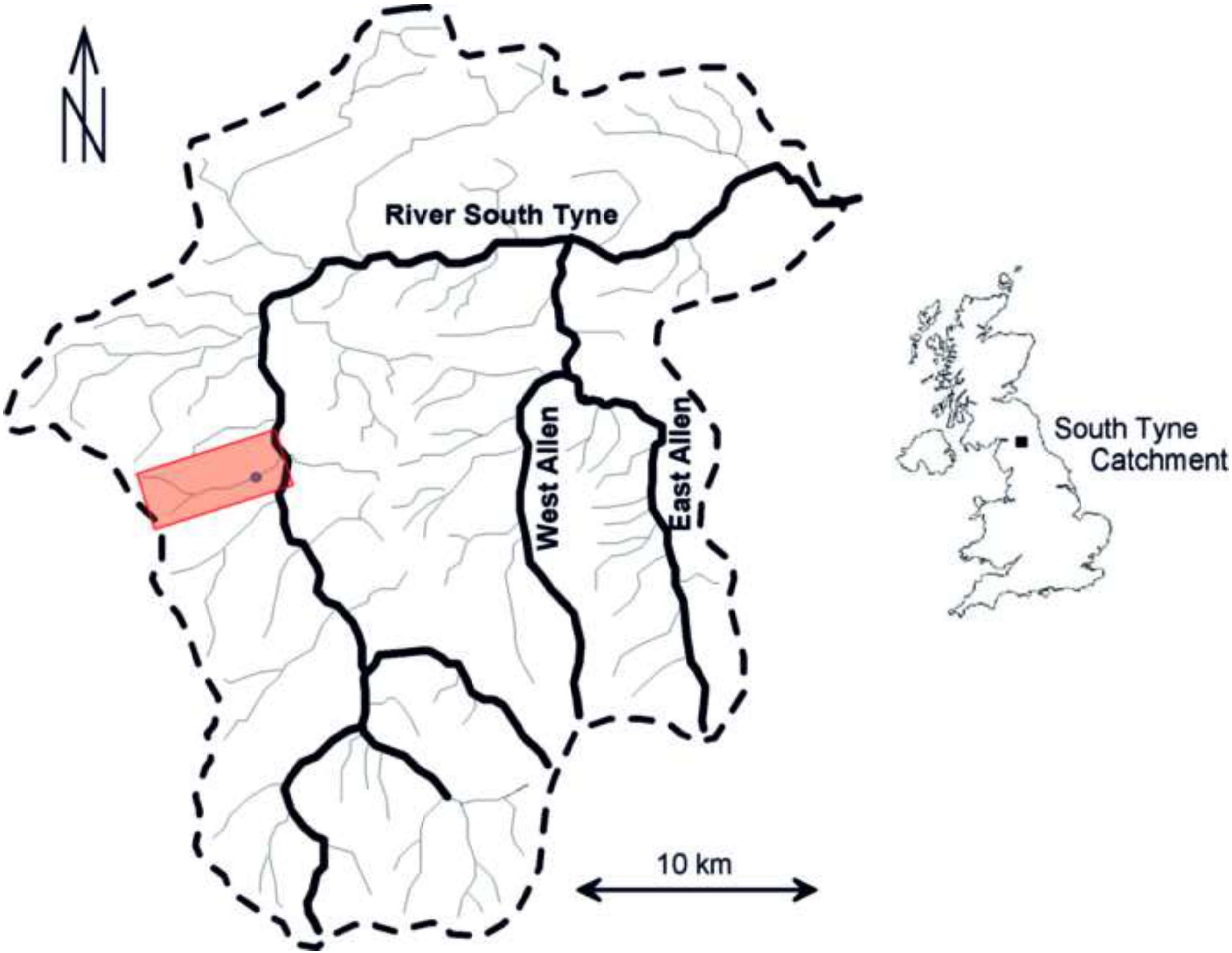

Figure 2 (Colour)
Click here to download high resolution image

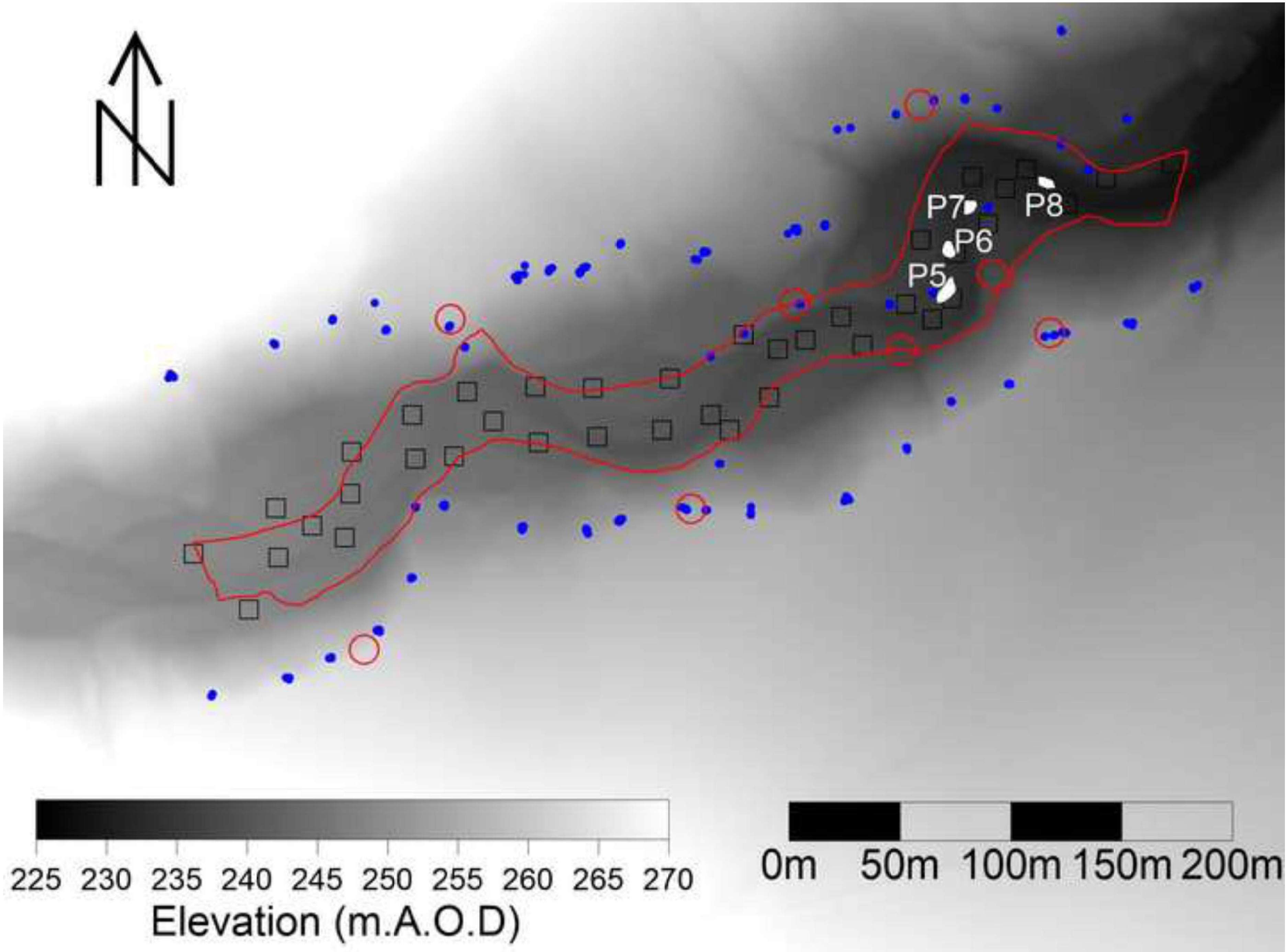

Figure 3 (Colour)
Click here to download high resolution image

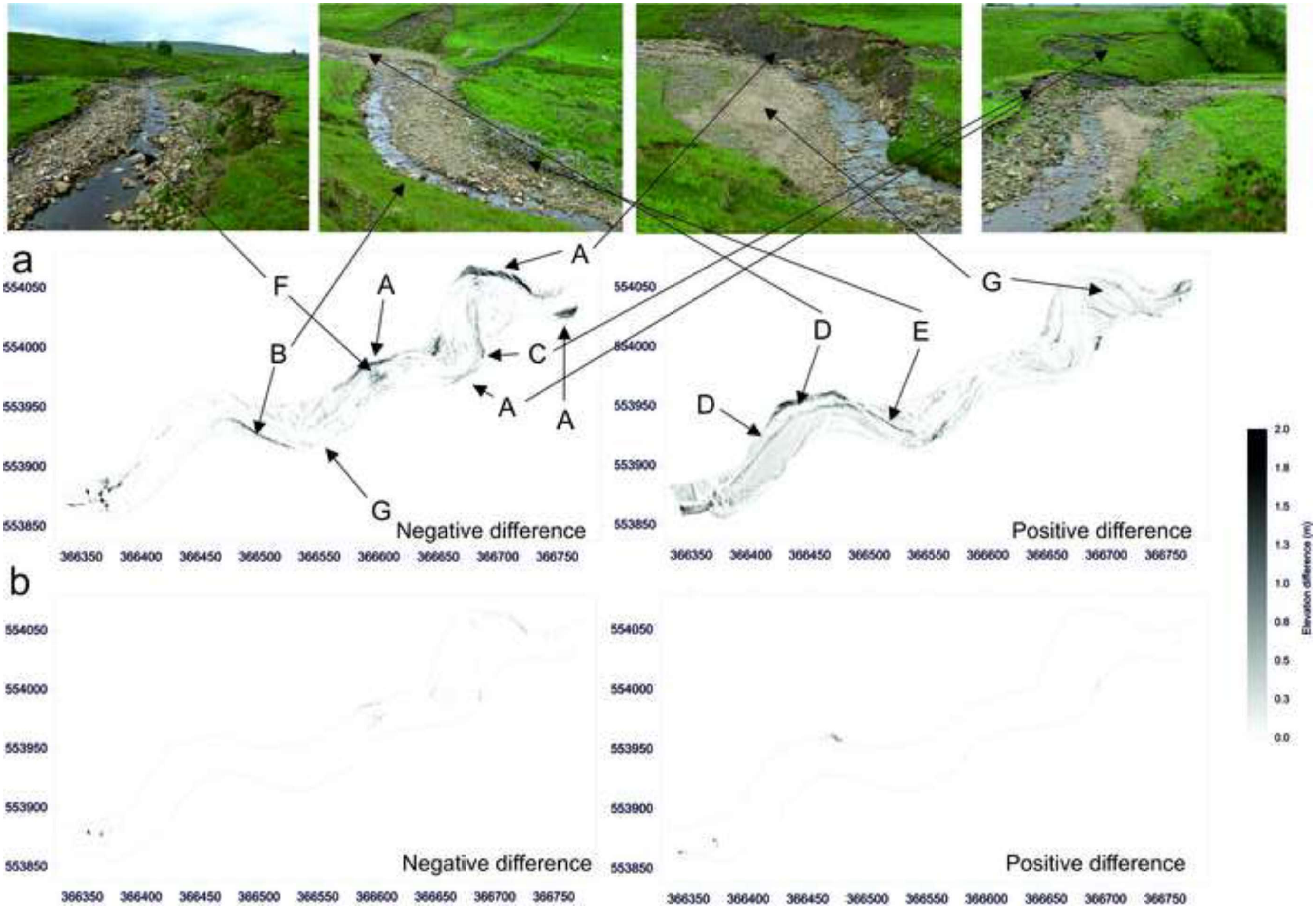

Figure 6 (Colour)
Click here to download high resolution image

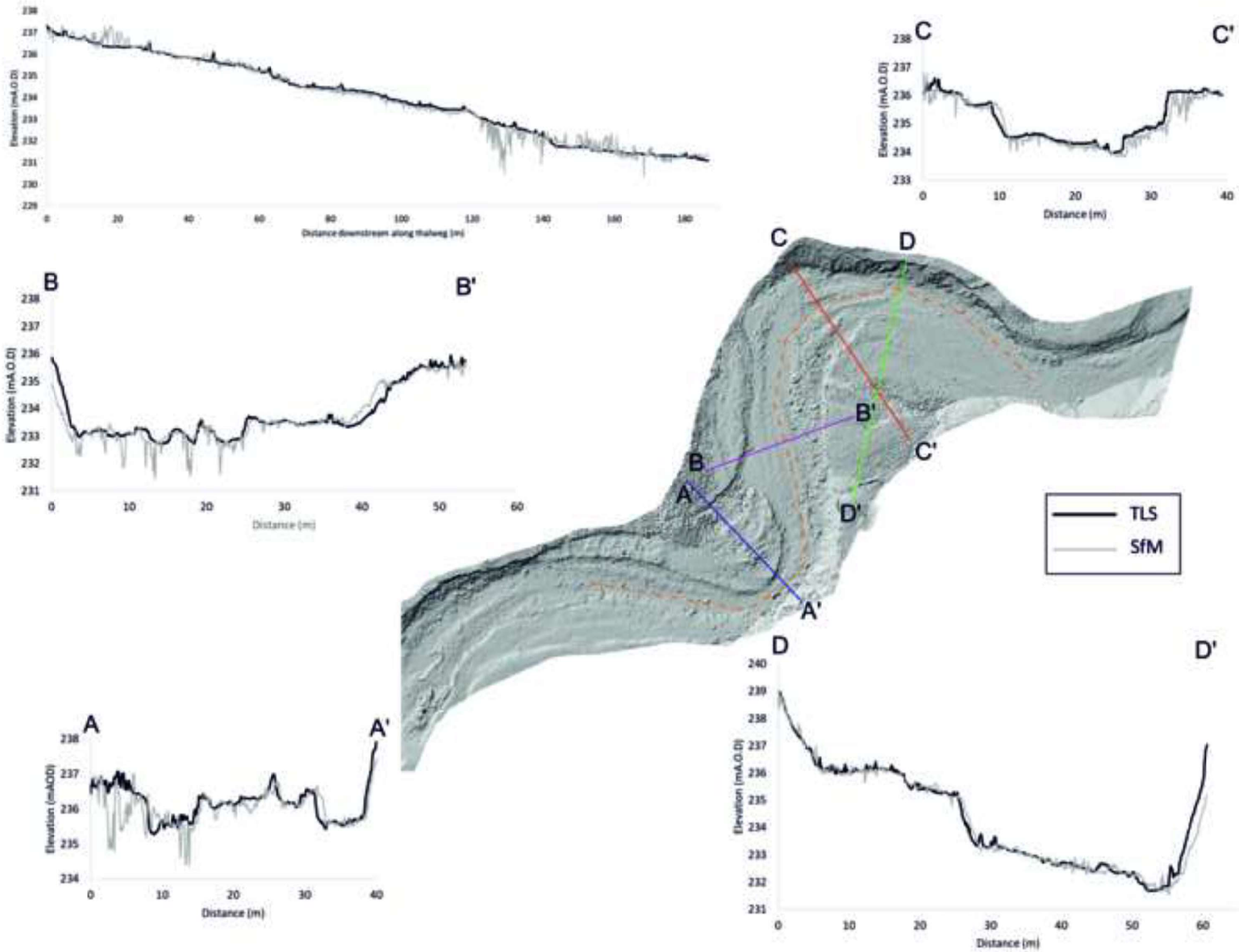

Figure 7 (Colour)
Click here to download high resolution image

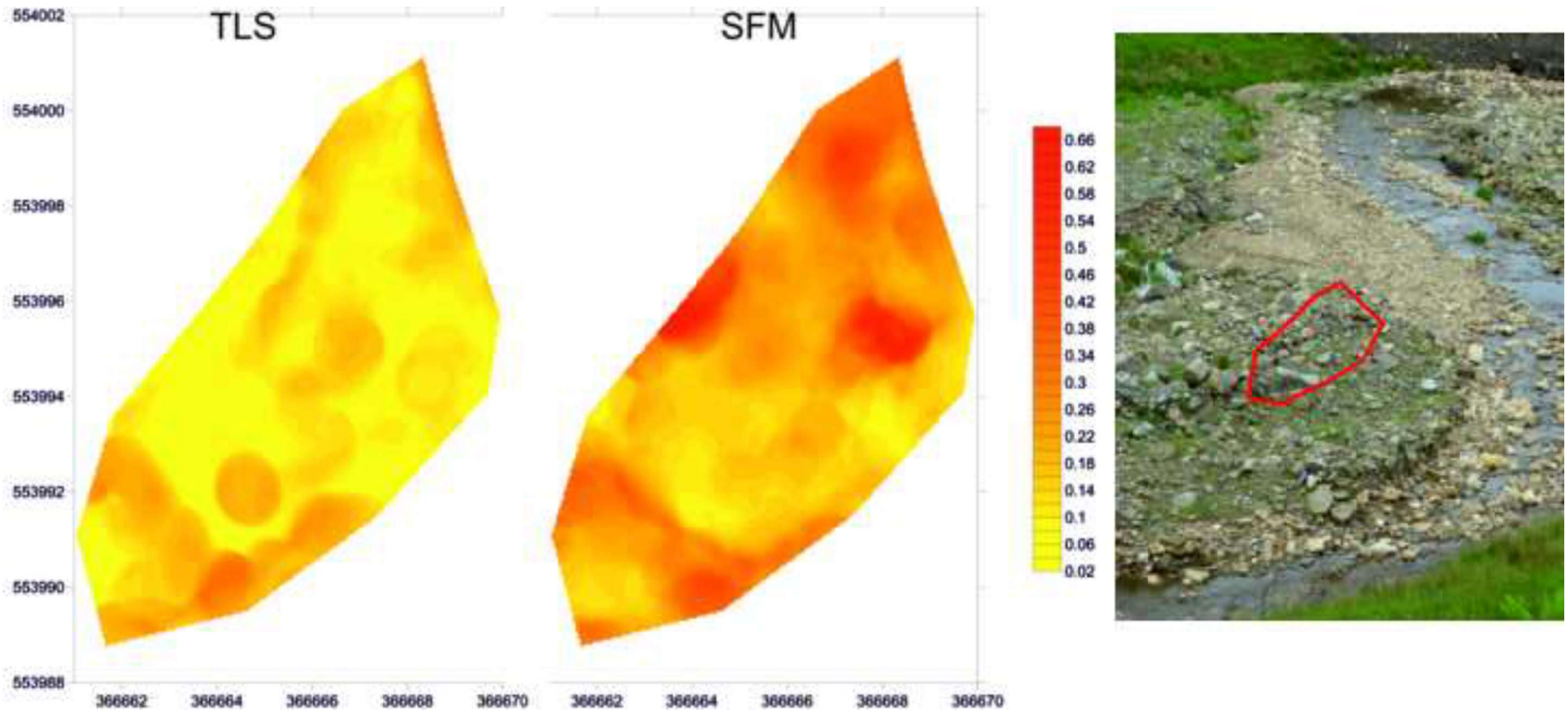

Figure 8 (Colour)
Click here to download high resolution image

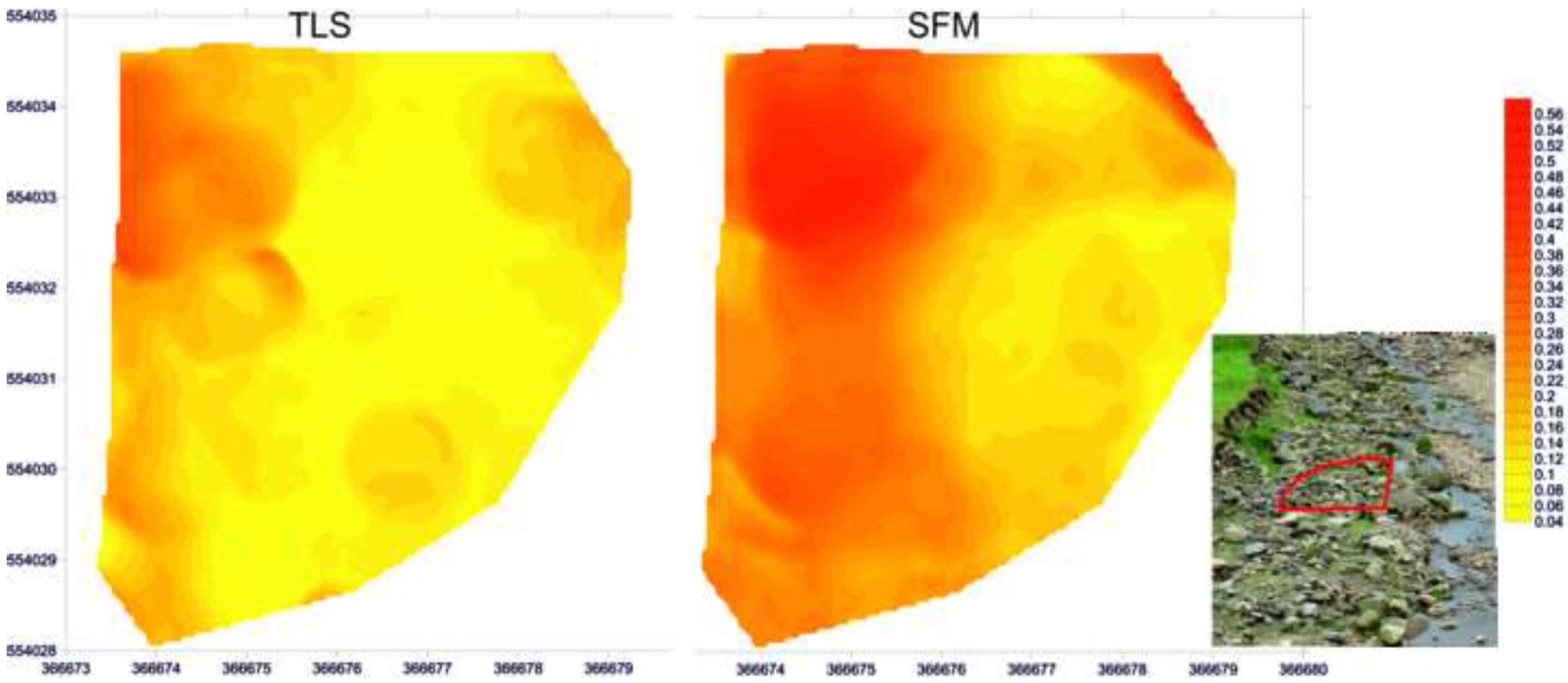

Figure 9 (Colour)

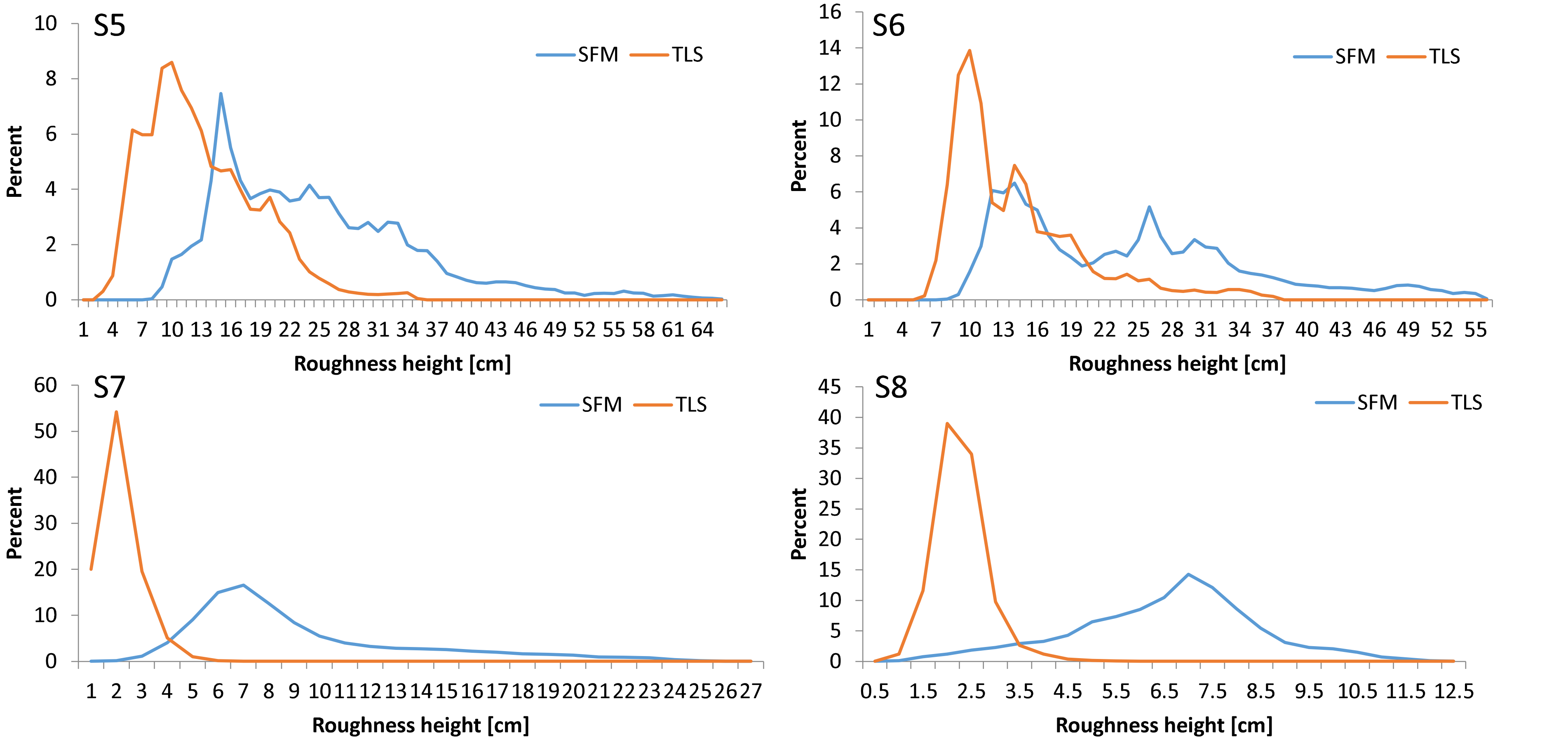

Figure 10 (Colour)
Click here to download high resolution image

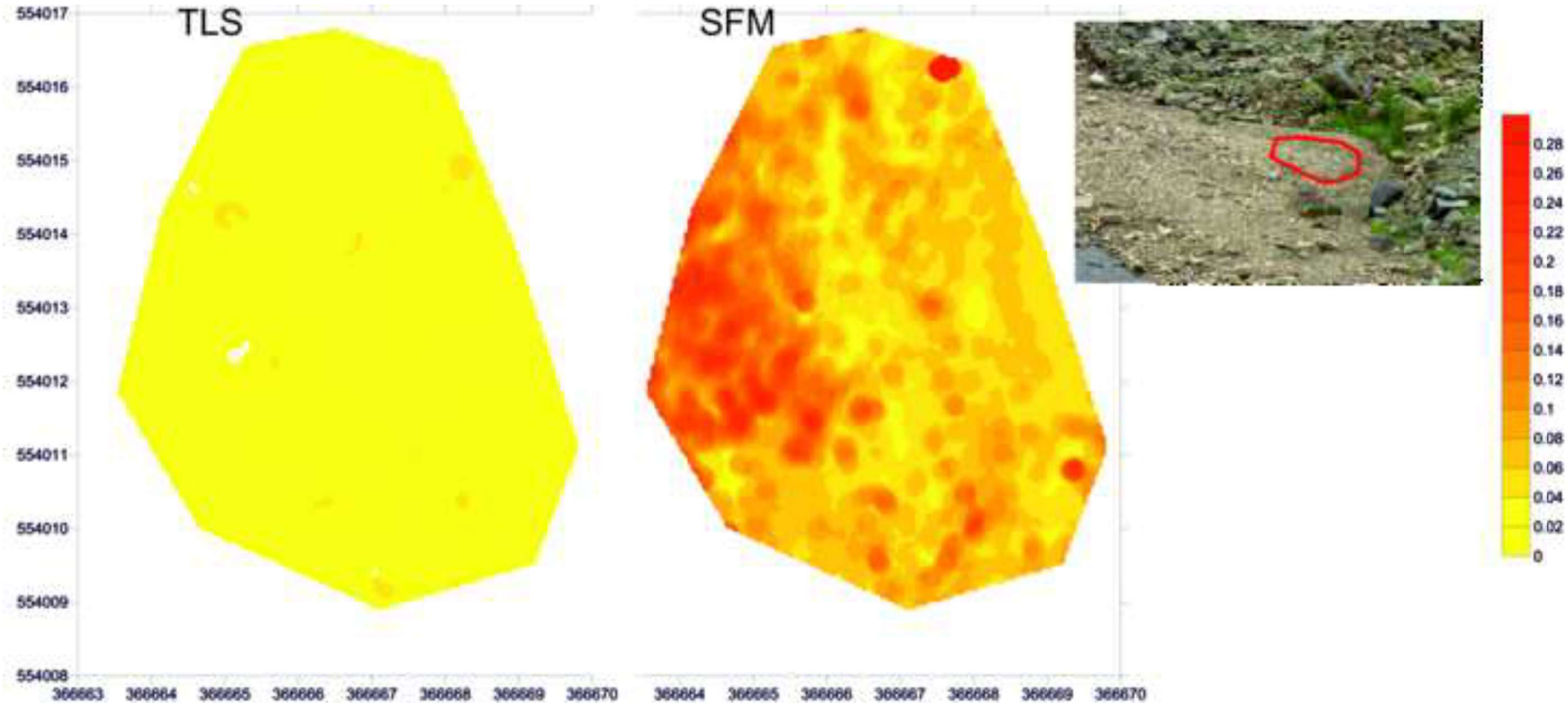

Figure 11 (Colour)
Click here to download high resolution image

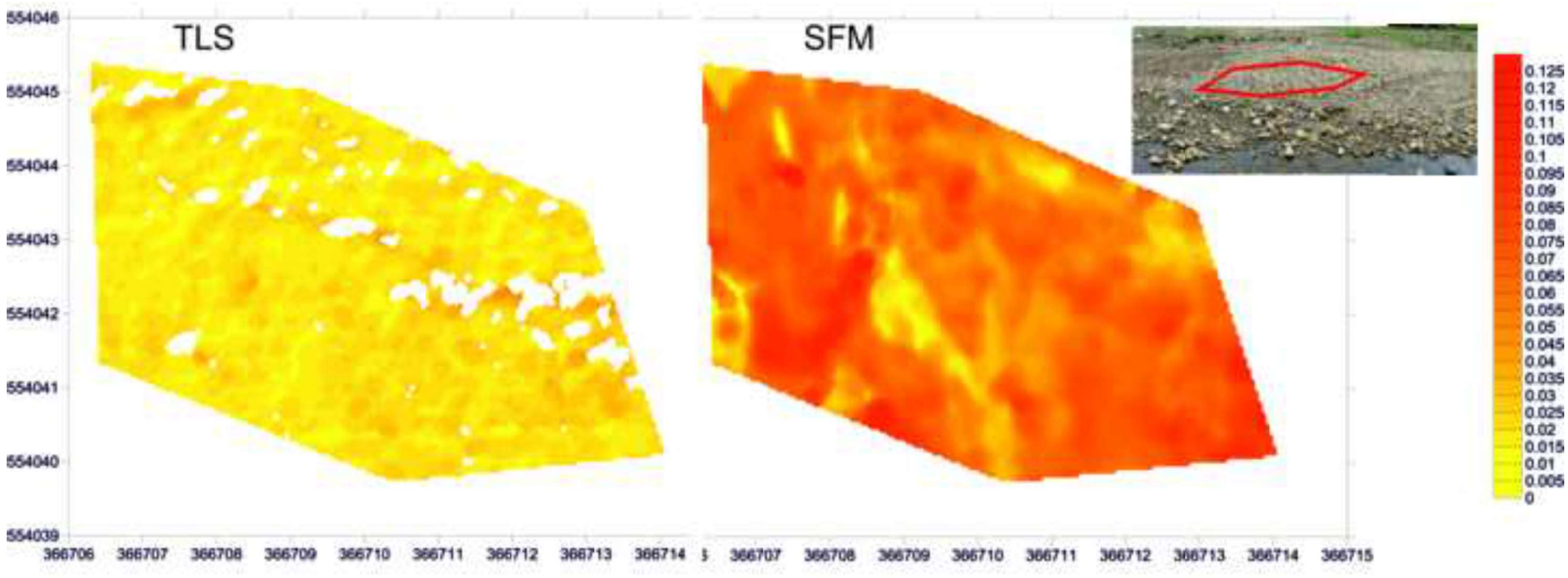

Figure 4
Click here to download high resolution image

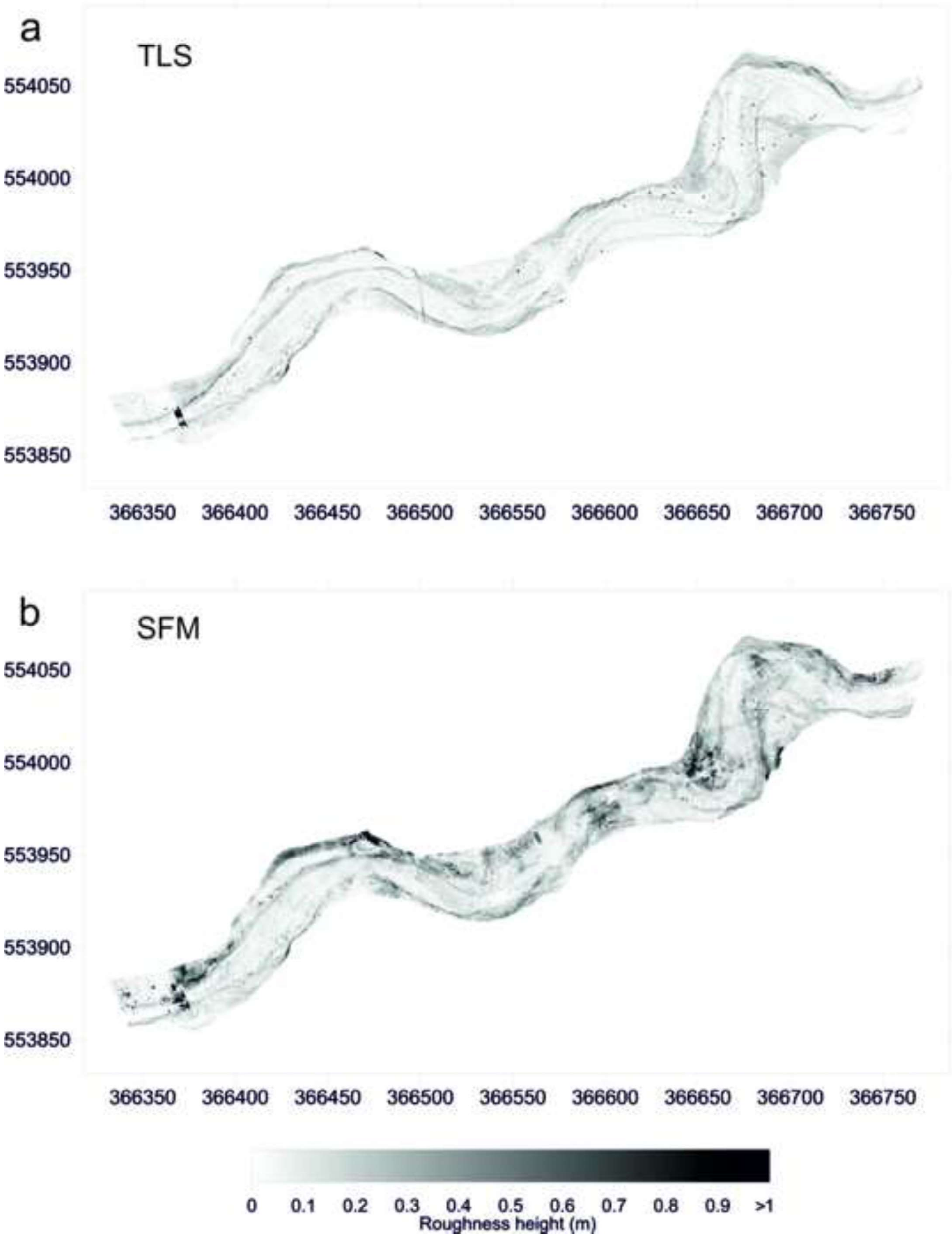

Figure 5

Click here to download high resolution image